Anthropogenic aerosols offsetting ocean warming less efficiently since the 1980s

Taimoor Sohail[1,2], Damien B. Irving[3], Jan D. Zika[1,2,4]and Jonathan M. Gregory[5]

[1]School of Mathematics and Statistics, University of New South Wales, Sydney, Australia
[2]Australian Center for Excellence in Antarctic Science, University of New South Wales, Sydney, Australia
[3]Commonwealth Scientific and Industrial Research Organisation (CSIRO), Hobart, Australia
[4]UNSW Data Science Hub (uDASH), University of New South Wales, Sydney, Australia
[5]Department of Meteorology, University of Reading, Reading, United Kingdom

Key Points:

- Since 1980, aerosol-driven ocean cooling has decelerated substantially, alongside a drop in ocean heat uptake efficiency.
- The drop in ocean heat uptake efficiency is limited to the tropics, which have equilibrated to sustained aerosol-driven radiative forcing.
- Air-sea fluxes into the coldest fraction of the ocean continue to offset greenhouse gas-driven ocean warming.

Corresponding author: T. Sohail, t.sohail@unsw.edu.au

Abstract

Greenhouse gases and aerosols play a major role in controlling global climate change. Greenhouse gases drive a radiative imbalance which warms the ocean, while aerosols cool the ocean. Since 1980, the effective radiation felt by the planet due to anthropogenic aerosols has levelled off, global ocean cooling due to aerosols has decelerated, and greenhouse gas-driven ocean warming has accelerated. We explore the deceleration of aerosol-driven ocean cooling by quantifying a time- and spatially-varying ocean heat uptake efficiency, defined as the change in the rate of global ocean heat storage per degree of cooling surface temperature. In aerosol-only simulations, ocean heat uptake efficiency has decreased by 69% since the 1900s. The tropics and sub-tropics have driven this decrease, while the coldest fraction of the ocean continues to sustain cooling and high ocean heat uptake efficiency. Our results identify a growing trend towards less efficient ocean cooling due to aerosols.

Plain Language Summary

The composition of the atmosphere has a major impact on our climate. Greenhouse gases warm the planet, while aerosols (i.e., suspensions of particles in the atmosphere) cool the planet, and most of this change is absorbed by the oceans. Since 1980, the rate of cooling of the planet due to aerosols has plateaued. In the past few decades, the ocean has begun to equilibrate to this change, and this work explores where and when this equilibration has occurred in the ocean based on global climate models. To understand this change, we use an 'ocean heat uptake efficiency' metric which describes how much additional heat builds up in the ocean for a given degree of surface temperature gain (or loss). We find that the ocean is cooling more slowly given a degree of surface cooling due to aerosols compared to the pre-1980s. This change is largely driven by the tropics and sub-tropics, where the ocean has stopped cooling in response to aerosol-driven negative surface temperatures. Polar and sub-polar regions, however, continue to cool due to aerosols. These changes are occurring alongside accelerating greenhouse gas-driven warming, suggesting that the relative role of aerosols in cooling our climate is weakening.

1 Introduction

Variations in the composition of the earth's atmosphere, namely, changing concentrations of greenhouse gases, aerosols and ozone, cause anthropogenic climate change. Greenhouse gases (GHGs) primarily inhibit loss of heat to space, and thus warm the climate system. The ocean absorbs a large proportion of the heat that consequently accumulates. A recent estimate suggests that approximately 89% of the excess heat in the climate system has been absorbed by the global oceans since 1970 (Schuckmann et al., 2020). Anthropogenic aerosols (AAs) cool the climate system (Ramanathan et al., 2001; Gleckler et al., 2006), and thus offset some of the GHG-driven ocean warming. They also introduce spatial heterogeneity into the ocean warming pattern (Delworth et al., 2005; D. B. Irving et al., 2019).

In order to understand the effect of GHGs and AAs on the ocean and climate, single-forcing simulations have been conducted by the Detection and Attribution Model Intercomparison Project (DAMIP) (Gillett et al., 2021), which is part of the Coupled Model Intercomparison Project (phase 6; CMIP6; Eyring et al. (2016)). In DAMIP, coupled atmosphere–ocean three-dimensional climate models are integrated from 1850 to 2014 in separate experiments forced by historical atmospheric concentrations of anthropogenic GHGs (*GHG-only*), aerosols (*AA-only*) and natural forcings (volcanic aerosol and variability in solar irradiance) individually, to compare their impact on the climate system (Gillett et al., 2016). The single-forcing simulations are compared with the standard CMIP6 historical experiment which includes all forcings together. Past research with DAMIP simu-

lations has shown that GHG-driven ocean warming has been offset by aerosols across a range of depths in an ensemble of climate models (Bilbao et al., 2019). This offsetting effect is stronger in the Northern Hemisphere than the Southern Hemisphere due to uneven aerosol concentrations in the atmosphere (D. B. Irving et al., 2019).

Since 1980, however, the aerosol-driven change in top-of-atmosphere net downward radiative flux, or effective radiative forcing (ERF), has levelled off at approximately -1W/m^2 relative to the pre-industrial climate (allowing for atmospheric adjustments) (C. J. Smith et al., 2021). In contrast, the GHG-driven effective radiative forcing has continued to grow, reaching over 2 W/m^2(relative to the pre-industrial climate) by 2014 (C. J. Smith & Forster, 2021). As a result of this ERF stabilisation, ocean cooling due to aerosols has plateaued in the top 2000m of the ocean, while GHG-driven warming has continued to accelerate (Lyu et al., 2021). Assuming this trend continues in the future, Lyu et al. (2021) produced future projections of top-2000m ocean heat content that are purely GHG-driven. However, the deep ocean adjusts to atmospheric changes on relatively long timescales, so the impact of the levelling off of aerosol-driven ERF on the *global* ocean heat uptake (that is, including the portion of the ocean deeper than 2000m) remains unclear. In general, it is unclear which regions of the ocean have equilibrated to the approximately constant aerosol ERF since 1980.

Changes in ocean heat content due to GHGs and aerosols may be expressed in terms of the 'ocean heat uptake efficiency' (in W m^{-2} K^{-1}), defined as the change in the rate of storage of heat by the global ocean per degree of change in the global-mean surface temperature (e.g., Raper et al. (2002); Kuhlbrodt and Gregory (2012)). For a given model, this diagnostic is a single number which measures the response of the physical mechanisms driving ocean heat uptake in that model. Typically, ocean heat uptake efficiency has been quantified in strongly forced (i.e., 1% CO_2 or abrupt-4×CO_2) coupled climate models (Kuhlbrodt & Gregory, 2012; Exarchou et al., 2015). Despite its utility in understanding past and future climate change, a similar estimate of ocean heat uptake efficiency has not been produced for simulated historical climate change.

In this work, we explore aerosol-driven changes to the heat content tendency budget and their constituent processes and heat uptake efficiency in a suite of CMIP6 simulations. In section 2, we lay out the diagnostics used in the analysis, and in section 3, we detail the models used in the study. Finally, in section 4 we explore the temporal and spatial change in heat content and heat uptake efficiency, followed by a discussion and summary of the results in section 5.

2 Theory

2.1 Global diagnostics

We begin by exploring the response of the global ocean to changing surface air temperatures and ERF since 1850. The globally-integrated ocean heat content is calculated from the three-dimensional temperature field $\Theta(x, y, z, t)$:

$$\mathcal{H}(t) = \rho_0 C_p \int \Theta(x, y, z, t) d\mathcal{V}, \tag{1}$$

where $\mathcal{V}$ is the volume, ρ_0 is the density and C_p is the specific heat capacity of seawater.

The effective radiative forcing is sourced directly from C. J. Smith and Forster (2021) (see their figure 1d and h for equivalent plots for GHG-only and AA-only runs, respectively). C. J. Smith and Forster (2021) calculate ERF by applying the linearised energy balance equation for the Earth to a broad suite of CMIP5 and CMIP6 models: $\Delta F = \Delta N_{TOA} - \lambda \Delta T_a$, where F is the effective radiative forcing, N_{TOA} is the top-of-atmosphere

energy imbalance, T_a is the mean surface air temperature (relative to pre-industrial), and λ is the climate feedback parameter. We opt to source the values of ERF directly from C. J. Smith and Forster (2021) because their methodology enables us to track changes to ERF over the entire historical period.

2.2 Ocean heat uptake efficiency

For timescales greater than about a year, we may assume that that all of the heat storage in the earth system occurs in the ocean (Palmer & McNeall, 2014). In this case, ocean heat content tendency can be related to global-mean surface air temperature change T_a through the ocean heat uptake efficiency, as:

$$N/A_T = \kappa T_a, \tag{2}$$

where $N = \partial\mathcal{H}(t)/\partial t$ is the rate of ocean heat content change (in W), A_T is the total surface area of earth (in m^2) and κ is the ocean heat uptake efficiency (in $Wm^{-2}K^{-1}$). Typically, κ is conceived as a single number for a given model which captures all of the ocean heat uptake processes of the model, and does not depend on time or the nature of the forcing. However, here we do not assume that κ is a single, fixed value characteristic of a specific model, and instead, we use κ to characterise the response of model heat content to changing surface air temperature over different time periods and over different layers of the ocean. These diagnostics enable us to understand when, how and in which layers aerosols have modified the underlying temperature structure of the ocean in recent decades.

2.3 Layer-wise heat content tendency

In this work, we track changes to the ocean heat content in depth layers, as done by Bilbao et al. (2019). Ocean heat content as a function of depth (in Jm^{-3}) is calculated by horizontally integrating the global temperature field:

$$\mathcal{H}(z,t) = \rho_0 C_p \int\int \Theta(x,y,z,t)dxdy, \tag{3}$$

We also investigate heat content in temperature-percentiles, following Sohail et al. (2021) and Holmes et al. (2022), to complement the depth-based analysis. Temperature-percentiles are defined in terms of the cumulatively-integrated ocean volume, from hot to cold, and represent the warmest x% of the ocean by volume. The temperature $\Theta^*(p,t)$ of temperature-percentile p (between 0 and 100) is defined such that p% of the ocean volume is warmer than $\Theta^*(p,t)$, i.e.,

$$\int_{V_T} W(Theta(x,y,z,t) - Theta*(p,t))dxdydz = 0.01pV_T, \tag{4}$$

where V_T is the total volume of the ocean, and the function $W(\delta) = 1$ for $\delta > 0$, and $W(\delta) = 0$ for $\delta <= 0$.

Temperature-percentiles provide a complementary perspective to existing water mass-based methods of tracking property changes (e.g., at constant absolute temperature), as detailed in Sohail et al. (2021); Holmes et al. (2022); Sohail et al. (2022). By tracking changes to the warmest x% of the ocean by volume, we:

1. Directly compare different models or observational products which may be uniformly warmer or cooler, but have the same cumulative volume distribution in percentile space.

2. Remove the effect of uniform warming or cooling over time, which would change the outcrop location of isotherms, making tracing property changes to a surface region more challenging.
3. Derive a simple heat content tendency budget where heat content tendency is a consequence of surface fluxes and mixing only (see Sohail et al. (2021) for further information).

Ocean heat content (in Jm^{-2}) of the part of the ocean colder than percentile p is calculated as:

$$\mathcal{H}(p,t) = 0.01 V_T \rho_0 C_p \int_0^p \Theta^*(p',t) dp', \tag{5}$$

where p is a given temperature-percentile, V_T is the total volume of the ocean, and $\Theta^*(p,t)$ is the temperature at a given percentile. From equation (4), the volume bounded by a temperature-percentile surface and the domain boundary is $0.01pV_T$. To ease in the visualisation of the results, we plot our results in terms of the time-mean temperature of a given percentile, $\overline{\Theta^p}$.

In temperature-percentiles, the ocean heat content tendency, $\partial\mathcal{H}(p,t)/\partial t$, is the sum of surface fluxes and mixing, $\partial\mathcal{H}(p,t)/\partial t = \mathbf{Q}(p,t) + \mathcal{M}(p,t)$. There is no term for advection (that is, large-scale adiabatic transport in physical space but not in Θ^* space), which does not change the distribution of volume as a function of temperature. Thus, we can not only diagnose the temperature-percentile layers where ocean heat content changes the most, but also the surface fluxes and mixing that contribute to this change.

3 Models

We analyse temperature and surface fluxes in nine climate models from DAMIP single-forcing experiments and their CMIP6 historical simulations. In order to limit the influence of model internal variability on ocean heat content tendency results, we take an ensemble mean across all ensemble members available for each model. For the nine models analysed, between two and 15 ensemble members are archived, resulting in a total of 48 ensemble members. Further details of the models analysed and their associated ensemble members are provided in the Supplementary Materials (Table S1).

We analyse the monthly-averaged ocean potential temperature (*thetao*), surface air temperature (*tas*) and net downward surface heat flux (*hfds*) from January 1850 to December 2014 in the DAMIP and CMIP6 simulations, also using surface grid cell area (*areacella*) and ocean grid cell volume (*volcello*). Ocean heat content in temperature percentiles $\mathcal{H}(p,t)$ is calculated by volume-integrating the three-dimensional temperature field Θ as a function of temperature percentile, p (Eq 5).

Heat content tendency N is calculated for a given temperature-percentile or depth layer or for the global ocean by taking the regression slope of ocean heat content against time in decadal windows, to obtain a quantity in J m^{-2}. The ocean heat uptake efficiency is calculated as N divided by T_a and by global surface area. The global surface heat flux is calculated by integrating the global area-mean of the two-dimensional surface heat flux field cumulatively in temperature-percentile. The result is cumulatively time-integrated and $\mathbf{Q}(p,t)$ is recovered as the regression slope of the time-integral against time in decadal windows. In this analysis, we assume the density of sea water is ρ_0 =1035 kgm^{-3}, and its specific heat capacity C_p = 4000 J kg^{-1} K^{-1}, unless directed otherwise by modelling groups.

Following D. Irving et al. (2020), Sohail et al. (2021) and Sohail et al. (2022), model drift is removed from all variables of interest by subtracting a fit as a function of time

during some reference simulation, in order to exclude any effect of drift on forced trends and the global ocean heat budget. For GHG-only and AA-only DAMIP simulations, which do not include natural forcing variations, we use a cubic fit to the 500 years of the pre-industrial control (*piControl*), which likewise has no natural forcing variation. A cubic fit is selected to ensure that centennial-scale drift is captured without overfitting onto modes of natural variability. For the CMIP6 historical simulations, a linear fit of the historical natural (*hist-nat*) simulations from the DAMIP single-forcing experiments is used, because the historical simulation *does* include historical natural forcings, and we wish to remove the long-term drift they cause, following Silvy et al. (2020). A linear fit is sufficient for this shorter (165 year) time series.

In the decades from 1995 to 2014, where the slowdown of aerosol-driven cooling is most evident, we focus on a single model (ACCESS-CM2) as an example, for which more detailed ocean heat budget tendency diagnostics are available (Bi et al., 2020). These diagnostics enable us to distinguish between the mixing mechanisms, shortwave redistribution and surface heat and volume fluxes that are driving ocean heat content change. Specifically, we diagnose the role of vertical mixing, numerical mixing, neutral diffusion, surface heat fluxes from surface volume fluxes, penetrative shortwave heating, total surface heat fluxes and other miscellaneous mixing on the ocean heat content in the AA-only and GHG-only runs of the ACCESS-CM2 model. As above, all heat content diagnostics are surface- or volume-integrated onto temperature percentiles and de-drifted from the piControl run. Tendencies are calculated from regression slopes in each percentile layer against time over the 1994 to 2014 time period. The discussion and results of this single-model analysis are presented in Figure S1 of the Supplementary Materials.

4 Results

We begin by exploring the global effective radiative forcing, surface air temperature and ocean heat content in the AA-only, GHG-only and historical (i.e. all forcings) simulations. Across all models, the GHG-only simulations exhibit a rapid acceleration in ERF, T_a and N since 1850 (figure 1a - c). However, the AA-only simulations have a different ocean and ERF response. As mentioned earlier, the ERF due to aerosols has plateaued since the 1980s at sustained levels below pre-industrial, as shown in figure 1a. This is largely mimicked by the surface air temperature field which has plateaued (figure 1b). By contrast, although the rate of ocean cooling has slowed, ocean heat content has not stabilised (see figure 1c). This could be due to the fact that the ocean equilibrates to changing surface forcing over long (decadal or greater) timescales, which have not yet been reached (Yang & Zhu, 2011). There may also be compensation in ocean heat content occurring between different oceanic regions, such that ocean warming in one region is offset by cooling elsewhere.

Figure 1d - f shows the quantities N, T_a and κ, which are related by equation (2), in the GHG- and AA-only and historical simulations in decadal time windows since 1855. Global ocean heat content tendency, N, has continued to grow since the 1980s in the GHG-only simulations (figure 1d), reflecting the acceleration of ocean warming due to greenhouse gases. Aerosol-driven ocean cooling, on the other hand, has begun to decelerate since the 1980s, matching the stabilisation of ERF and mean surface air temperature during this time (figure 1e), and N has tended to become less negative since the 1970s. The historical OHC, N, T_a, and ERF (purple lines in figure 1a - e) are a linear combination of the AA-only, GHG-only and natural forcings (not shown).

Ocean heat uptake efficiency κ has qualitatively different GHG-only, AA-only and historical responses. Prior to 1900, inter-model variability in κ is extremely large in all simulations due to the small signal in N and T_a. This is especially true in the historical simulations, where a combination of a weak signal in N and T_a and higher inter-model variability leads to extremely uncertain estimates of κ until the 2000s and no discernible

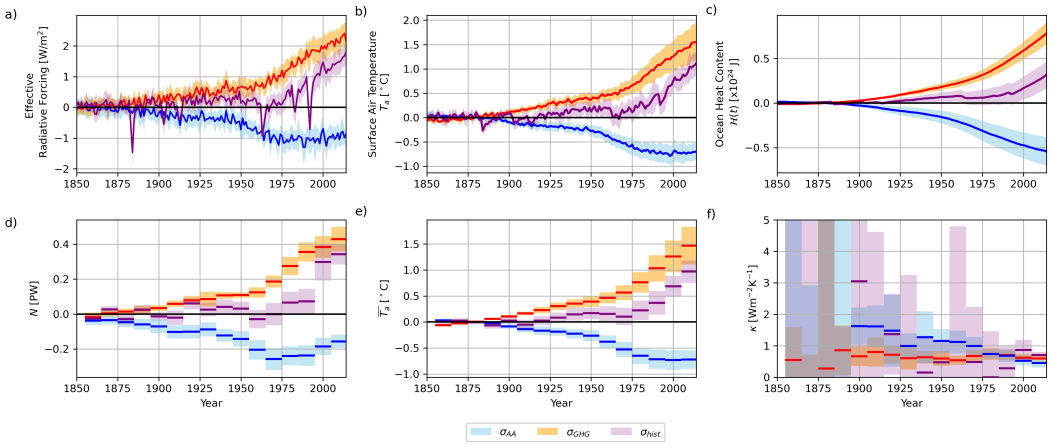

Figure 1. The multi-model-mean a) effective radiative forcing ERF (sourced from figure 1h of C. J. Smith and Forster (2021)), b and e) global-mean surface air temperature T_a, c) globally-integrated ocean heat content $\mathcal{H}$, d) globally-integrated ocean heat content tendency N, f) ocean heat uptake efficiency κ. All quantities are shown separately for GHG-only (orange), AA-only (blue) and historical (all-forcings, purple) simulations, and plotted relative to their 1850-1900 time-mean. (a-c) are annual means, (d-f) decadal means. The standard deviation (shaded regions) illustrates the inter-model variance of the nine model ensemble-means analysed.

trend (see purple lines and shading in figure 1f). In addition, the historical κ is not a linear combination of the two single forcing simulations. This non-linearity is inevitable, given that historical N and $\overline{T_a}$ *are* linearly additive combinations of GHG-only and AA-only, but with different κ.

In the GHG-only simulations, κ has remained largely stable since the 1900s, at $\sim$ 0.66W/m^{2}K, as shown in figure 1f. This value of κ is broadly consistent with previous estimates in strongly-forced climate models and observations (Winton et al., 2014; Kuhlbrodt & Gregory, 2012; Cael, 2022). In AA-only simulations, κ has exhibited a sustained decline since the 1900s, from $\sim$ 1.6W/m^{2}K to $\sim$ 0.5W/m^{2}K. The inter-model variability in this AA-only estimate has sharply reduced since the 1980s, signalling that the ocean in most model members is exhibiting this drop in ocean heat uptake efficiency. Prior to 1970, AA-only ocean heat uptake efficiency is greater than that in the GHG-only simulations before becoming indistinguishable in more recent decades. This difference may be due to the fact that a large proportion of ocean cooling occurs in the rapidly ventilating sub-polar and polar regions in the AA-only simulations, as indicated in the coldest temperature-percentiles in figure 2.

Our results show that, globally, both the rates of ocean cooling and the ocean heat uptake efficiency have dropped in response to aerosols (blue lines in figure 1d and f). In order to distinguish *in which layers* this drop occurs, we calculate the layer-wise ocean heat uptake, following equations (5) for temperature-percentiles and (3) for depth layers in decadal time windows (see figure 2a, b, e and f). The layer-wise κ is then $N(p,t)/\overline{T_a}$ in temperature-percentiles and $N(z,t)/\overline{T_a}$ in depth (figure 2c, d, g and h). Due to the different layer thickness in temperature-percentiles and depth, we cumulatively integrate from hot to cold or from top to bottom to enable a direct comparison.

The profiles of the multi-model-mean ocean heat content tendency in temperature-percentiles (or depth) are shown in figure 2a and b for GHG-only and figure 2e and f for AA-only simulations, from 1945 to 2014. The ocean heat content tendency in GHG-only

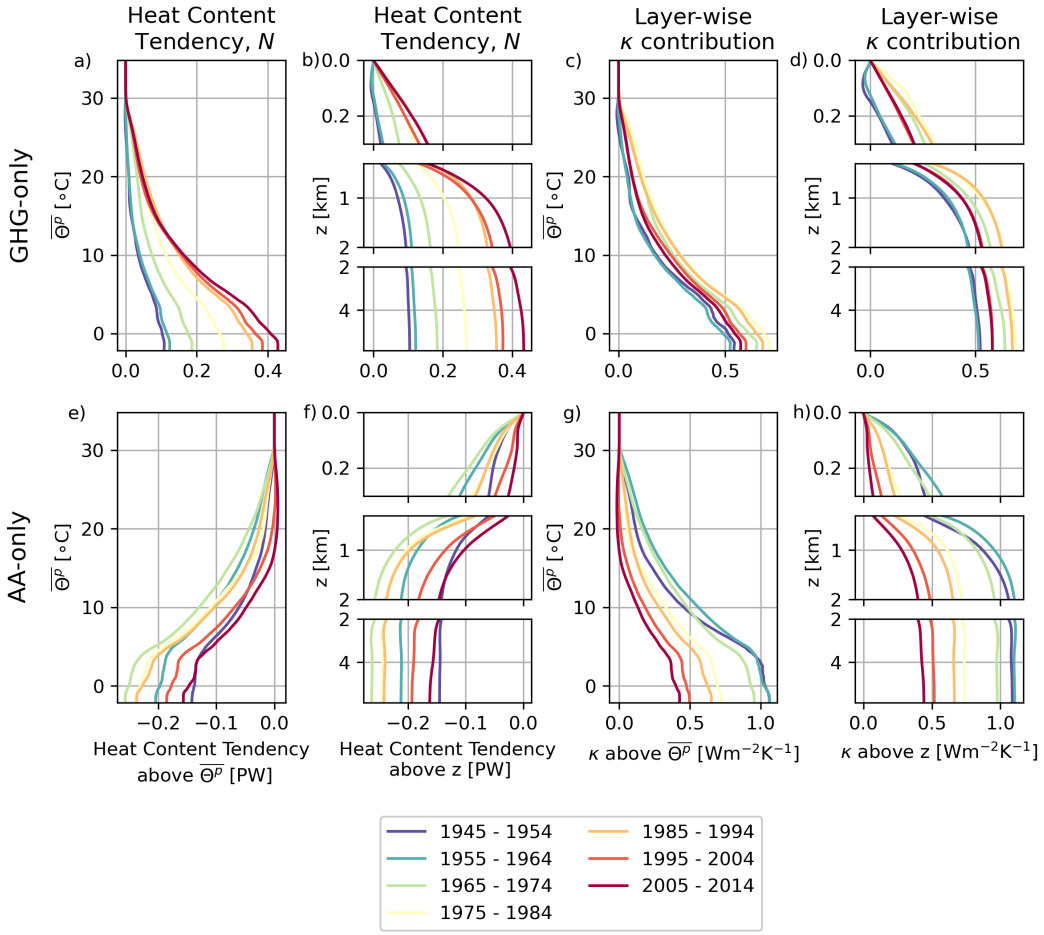

Figure 2. The multi-model-mean layer-wise ocean heat content tendency, N (a, b, e and f), and ocean heat uptake efficiency contribution, κ (c, d, g and h), in temperature-percentile (a, c, e and g) and depth (b, d, f and h) layers, across decadal windows from 1945-1954 (blue) to 2005-2014 (red). The top row shows the GHG-only simulation results (a - d), while the bottom row shows the AA-only simulation results (e - h). To ease in visualisation, we plot our temperature-percentile results in terms of the time-mean temperature of a given percentile surface, $\overline{\Theta^p}$.

simulations shows a warming across all temperature-percentile and depth classes (figure 2a and b).

In an aerosol-forced ocean, prior to the 1980s, all water masses are cooling, and the $\overline{\Theta^p} > 5^\circ$ C (z<2 km) layer emerges as a key zone of ocean cooling (see figure 2e and f). After the 1980s, the rate of cooling declines, and there is warming after the 1990s above 20°C. Since warming cannot be seen at any depth, even at the surface, we infer that, soon after the plateauing of aerosol ERF, cooling of the upper ocean ceases in the warm tropics and subtropics, where equilibration to forcing is rapid, while continuing at colder polar and sub-polar regions and in the global mean. Cooling continues also in the deep ocean (i.e. $N < 0$) at all latitudes, as the effect of previously growing negative ERF continues to spread downwards.

The layer-wise κ (shown in figure 2c, d, g and h) shows that under continuously increasing GHG forcing (figures 2c-d) all layers make a fairly constant contribution to

ocean heat uptake efficiency, which initially increases and later decreases slightly. In contrast, for aerosol forcing (Figures 2g - h) the contribution is fairly constant until the ERF plateaus but subsequently declines at all levels. Since 1994, the tropics and sub-tropics (above 20°C) have stopped cooling in response to surface cooling (see orange and red lines in figure 2g). This is not seen in depth layers (figure 2h) due to the combination of surface tropics and sub-tropics with the surface polar and sub-polar regions.

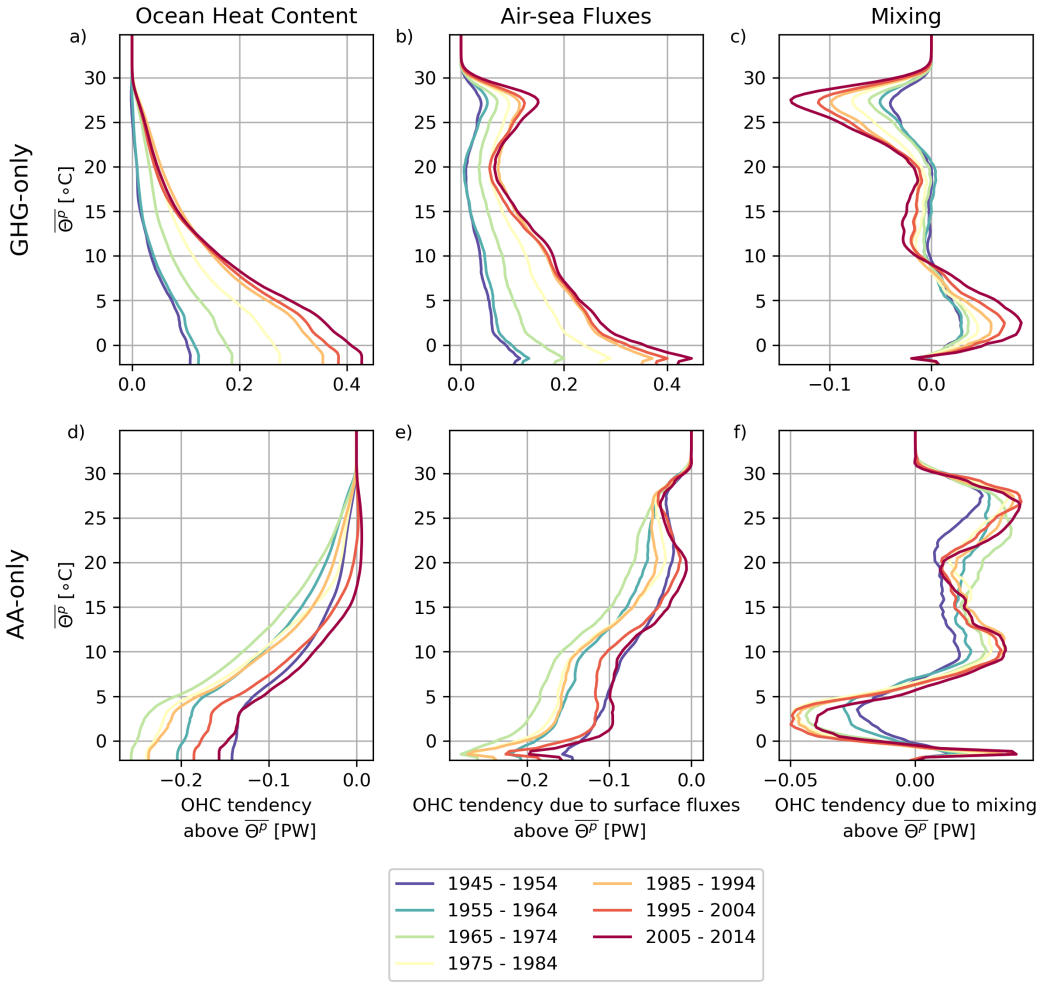

Figure 3. The multi-model-mean ocean heat content tendency (a and d), change in surface heat flux (b and e), and change in diathermal heat flux (c and f) in GHG-only (top row) and AA-only (bottom row) CMIP6 simulations, plotted in temperature-percentile space for decadal time windows from 1945 to 2014. Note that panels a) and d) are identical to panels a) and e) in figure 2. To ease in visualisation, we plot our results in terms of the time-mean temperature of a given percentile surface, $\overline{\Theta^p}$.

Air-sea heat fluxes can be diagnosed in temperature-percentiles from the DAMIP model outputs, and the diathermal mixing is calculated as the difference between the ocean heat content tendency and the change in surface heat flux, given that there are no other terms in the heat budget. Thus, in figure 3b and e, we present the ocean heat content tendency due to change in surface heat flux in the GHG-only and AA-only simulations, respectively, and in figure 3c and f we show the tendency due to change in diather-

mal mixing in the GHG-only and AA-only simulations. The GHG-only simulations show a growing heat flux into the warmest fraction of the ocean ($\overline{\Theta^p} > 27^\circ$ C) and parts of the sub-tropics and sub-polar ocean. Notably, there is a patch of surface cooling in the water masses aligning with $20 < \overline{\Theta^p} < 27^\circ$ C, corresponding with the location of the sub-tropical gyres in the ocean (not shown). The mixing tends to oppose the surface flux tendency in most water masses, except in the temperature-percentiles corresponding to the polar and sub-polar regions and deep ocean ($4 < \overline{\Theta^p} < 10^\circ$ C).

The surface heat flux in the AA-only simulations becomes increasingly negative for all temperature-percentile classes until the 1980s. Following the stabilisation of the AA-only ERF, surface flux-driven cooling comes to equilibrium with the stabilised forcing above $\overline{\Theta^p} = 20^\circ$ C. Similarly to the GHG-only runs, a warm-cold dipole forms over the temperature-percentiles corresponding to the sub-tropical gyres in the AA-only simulations. This warm-cold dipole is consistent with a shift of surface warming (or cooling) towards the warmest temperature-percentiles at the ocean surface. Air-sea cooling below $\overline{\Theta^p} = 20^\circ$ C, on the other hand, continues to drive a cooling at a constant rate despite the ERF stabilisation. This implies that AA-driven ocean cooling is sustained outside of the tropics and sub-tropics via air-sea fluxes.

Apart from the air-sea heat redistribution signal in the warmest temperature-percentiles (i.e., the bumps in figures 3b and e in the $20 < \overline{\Theta^p} < 27^\circ$ C layers), there is a strong qualitative similarity between the total OHC tendency and the OHC tendency due to the change in air-sea heat flux. This similarity suggests that surface heat uptake is transported mostly isothermally in the interior, consistent with the isopycnal analysis of (Saenko et al., 2021) and the isothermal analysis of (Sohail et al., 2021) in historical CMIP6 simulations.

Prior work from Exarchou et al. (2015); Saenko et al. (2021) has shown that high-latitude heat uptake is driven by vertical mixing and neutral diffusion in strongly warming climate models under idealised future forcing scenarios. In order to explore whether this is true in the CMIP6 experiments assessed here, we analyse the 1995-2014 time period in a single climate model - ACCESS-CM2 - for which detailed tendency budget terms are available. Our results corroborate this prior work, confirming that, in ACCESS-CM2, neutral diffusion (due to lateral eddies) and vertical mixing (likely due to convection) drive a significant amount of the ocean heat uptake in both the GHG-only and the AA-only simulations (see Figure S1 in Supplementary Materials). In addition, the mixing profiles in figure 3 (which are inferred as the residual of ocean heat content tendency and surface fluxes) match the explicitly diagnosed mixing in ACCESS-CM2. Prior work has established that the representation of high latitude ocean processes in CMIP6 models is highly uncertain (Heuzé, 2020), and our results emphasise the importance of better representing polar and sub-polar processes in future climate projections of ocean heat content.

5 Discussion

The temperature-percentile framework used in this work shows promise for use with other strongly-forced model simulations. The temperature-percentile framework enables more direct comparisons between models and observations which may have different mean states but have a similar volumetric temperature distribution. It also allows for large multi-model analyses by simplifying the heat budget and reducing the impact of drifting isotherms on the analysis of strongly-forced simulations, such as in future scenarios. On the other hand, the temperature-percentile framework collapses oceanic changes to a single dimension. We are thus unable to distinguish between hemispheric changes (likely important for aerosols, see D. B. Irving et al. (2019)), or across basins. New two-dimensional percentile methods, such as the partitioning method presented in Sohail et al. (2023), show

some promise in preserving spatial details in percentile space, and may be used to extend this analysis int eh future.

In this work, we have explored the slowdown in ocean cooling due to aerosols since 1980. We use a set of single-forcing DAMIP simulations (comprising nine climate models and 48 ensemble members in total) forced by greenhouse gases (GHGs) or anthropogenic aerosols (AA) to investigate the time period, layers and processes driving this deceleration in aerosol-driven ocean cooling. We find that, despite aerosols' historic role in suppressing warming due to GHGs, since 1980 the effective radiative forcing due to aerosols has stabilised and the ocean has begun to equilibrate to this new climate state. Globally, the AA-only ocean has begun to cool less rapidly, and the global ocean heat uptake efficiency, which represents the response of ocean heat content to a degree of surface warming or cooling, has dropped by 69%. These decelerating rates of cooling and reduced heat uptake efficiency have been confined to the tropics and sub-tropics, driven by warmer-than-usual air-sea fluxes. In contrast, in the coldest layers (corresponding to the polar and sub-polar regions), air-sea heat fluxes have continued to sustain ocean cooling and drive up ocean heat uptake efficiency. Thus, the polar and sub-polar regions can still be cooled efficiently in response to aerosol forcing, offsetting the relatively efficient ocean warming due to greenhouse gasses.

6 Open Research

The CMIP6 data used in this work is publicly available from ESGF: https://esgf-node.llnl.gov/search/cmip6/. The full list of CMIP6 models used as well as their corresponding ensemble members is provided in Table S1. The ACCESS-CM2 tendency diagnostics, binned into temperature-percentile space (see Supplementary Materials), are available via *Zenodo*: 10.5281/zenodo.8123005. Effective Radiative Forcing data and code for calculations are sourced directly from (C. Smith, 2021).

Acknowledgments

We acknowledge the World Climate Research Program, the CMIP6 climate modeling groups, the Earth System Grid Federation (ESGF), and the funding agencies supporting CMIP6 and ESGF. Modeling and analysis were undertaken with National Computational Infrastructure (NCI) facilities, supported by the Australian Government. This work is supported by the Australian Research Council (ARC) Centre of Excellence for Climate Extremes, the Australian Center for Excellence in Antarctic Science, the Centre for Southern Hemisphere Oceans Research and the ARC Discovery Project scheme (DP190101173).

References

Bi, D., Dix, M., Marsland, S., O'Farrell, S., Sullivan, A., Bodman, R., ... Heerdegen, A. (2020). Configuration and spin-up of ACCESS-CM2, the new generation Australian Community Climate and Earth System Simulator Coupled Model. *Journal of Southern Hemisphere Earth Systems Science*. doi: 10.1071/es19040

Bilbao, R. A. F., Gregory, J. M., Bouttes, N., Palmer, M. D., & Stott, P. (2019). Attribution of ocean temperature change to anthropogenic and natural forcings using the temporal, vertical and geographical structure. *Climate Dynamics*, *53*(9-10), 5389–5413. doi: 10.1007/s00382-019-04910-1

Cael, B. B. (2022). Ocean Heat Uptake Efficiency Increase Since 1970. *Geophysical Research Letters*, *49*(19). doi: 10.1029/2022gl100215

Delworth, T. L., Ramaswamy, V., & Stenchikov, G. L. (2005). The impact of aerosols on simulated ocean temperature and heat content in the 20th century. *Geophysical Research Letters*, *32*(24). doi: 10.1029/2005gl024457

Exarchou, E., Kuhlbrodt, T., Gregory, J. M., & Smith, R. S. (2015). Ocean Heat

Uptake Processes: A Model Intercomparison. *Journal of Climate*, *28*(2), 887–908. doi: 10.1175/jcli-d-14-00235.1

Eyring, V., Bony, S., Meehl, G. A., Senior, C. A., Stevens, B., Stouffer, R. J., & Taylor, K. E. (2016). Overview of the Coupled Model Intercomparison Project Phase 6 (CMIP6) experimental design and organization. *Geoscientific Model Development*, *9*(5), 1937–1958. doi: 10.5194/gmd-9-1937-2016

Gillett, N. P., Kirchmeier-Young, M., Ribes, A., Shiogama, H., Hegerl, G. C., Knutti, R., ... Ziehn, T. (2021). Constraining human contributions to observed warming since the pre-industrial period. *Nature Climate Change*, *11*(3), 207–212. doi: 10.1038/s41558-020-00965-9

Gillett, N. P., Shiogama, H., Funke, B., Hegerl, G., Knutti, R., Matthes, K., ... Tebaldi, C. (2016). The Detection and Attribution Model Intercomparison Project (DAMIP v1.0) contribution to CMIP6. *Geoscientific Model Development*, *9*(10), 3685–3697. doi: 10.5194/gmd-9-3685-2016

Gleckler, P. J., Wigley, T. M. L., Santer, B. D., Gregory, J. M., AchutaRao, K., & Taylor, K. E. (2006). Krakatoa's signature persists in the ocean. *Nature*, *439*(7077), 675–675. doi: 10.1038/439675a

Heuzé, C. (2020). Antarctic Bottom Water and North Atlantic Deep Water in CMIP6 models. *Ocean Science*, *17*(1), 59–90. doi: 10.5194/os-17-59-2021

Holmes, R. M., Sohail, T., & Zika, J. D. (2022). Adiabatic and Diabatic Signatures of Ocean Temperature Variability. *Journal of Climate*, *35*(5), 1459–1477. doi: 10.1175/jcli-d-21-0695.1

Irving, D., Hobbs, W., Church, J., & Zika, J. (2020). A Mass and Energy Conservation Analysis of Drift in the CMIP6 Ensemble. *Journal of Climate*, *34*(8), 3157–3170. doi: 10.1175/jcli-d-20-0281.1

Irving, D. B., Wijffels, S., & Church, J. A. (2019). Anthropogenic Aerosols, Greenhouse Gases, and the Uptake, Transport, and Storage of Excess Heat in the Climate System. *Geophysical Research Letters*, *46*(9), 4894–4903. doi: 10.1029/2019gl082015

Kuhlbrodt, T., & Gregory, J. M. (2012). Ocean heat uptake and its consequences for the magnitude of sea level rise and climate change. *Geophysical Research Letters*, *39*(18). doi: 10.1029/2012gl052952

Lyu, K., Zhang, X., & Church, J. A. (2021). Projected ocean warming constrained by the ocean observational record. *Nature Climate Change*, 1–6. doi: 10.1038/s41558-021-01151-1

Palmer, M. D., & McNeall, D. J. (2014). Internal variability of Earth's energy budget simulated by CMIP5 climate models. *Environmental Research Letters*, *9*(3), 034016. doi: 10.1088/1748-9326/9/3/034016

Ramanathan, V., Crutzen, P. J., Kiehl, J. T., & Rosenfeld, D. (2001). Aerosols, Climate, and the Hydrological Cycle. *Science*, *294*(5549), 2119–2124. doi: 10.1126/science.1064034

Raper, S. C. B., Gregory, J. M., & Stouffer, R. J. (2002). The Role of Climate Sensitivity and Ocean Heat Uptake on AOGCM Transient Temperature Response. *Journal of Climate*, *15*(1), 124–130. doi: 10.1175/1520-0442(2002)015⟨0124:trocsa⟩2.0.co;2

Saenko, O. A., Gregory, J. M., Griffies, S. M., Couldrey, M. P., & Dias, F. B. (2021). Contribution of Ocean Physics and Dynamics at Different Scales to Heat Uptake in Low-Resolution AOGCMs. *Journal of Climate*, *34*(6), 2017–2035. doi: 10.1175/jcli-d-20-0652.1

Schuckmann, K. v., Cheng, L., Palmer, M. D., Hansen, J., Tassone, C., Aich, V., ... Wijffels, S. E. (2020). Heat stored in the Earth system: where does the energy go? *Earth System Science Data*, *12*(3), 2013–2041. doi: 10.5194/essd-12-2013-2020

Silvy, Y., Guilyardi, E., Sallée, J.-B., & Durack, P. J. (2020). Human-induced changes to the global ocean water masses and their time of emergence. *Nature*

Climate Change, 1–7. doi: 10.1038/s41558-020-0878-x

Smith, C. (2021). chrisroadmap/cmip5-cmip6-forcing: Suppressed late-20th Century warming in CMIP6 models explained by forcing and feedbacks. Retrieved from `https://doi.org/10.5281/zenodo.5421581` doi: 10.5281/zenodo.5421581

Smith, C. J., & Forster, P. M. (2021). Suppressed Late-20th Century Warming in CMIP6 Models Explained by Forcing and Feedbacks. *Geophysical Research Letters*, *48*(19). doi: 10.1029/2021gl094948

Smith, C. J., Harris, G. R., Palmer, M. D., Bellouin, N., Collins, W., Myhre, G., ... Forster, P. M. (2021). Energy Budget Constraints on the Time History of Aerosol Forcing and Climate Sensitivity. *Journal of Geophysical Research: Atmospheres*, *126*(13). doi: 10.1029/2020jd033622

Sohail, T., Holmes, R. M., & Zika, J. D. (2023). Watermass Co-Ordinates Isolate the Historical Ocean Warming Signal. *Journal of Climate*, 1–40. doi: 10.1175/jcli-d-22-0363.1

Sohail, T., Irving, D. B., Zika, J. D., Holmes, R. M., & Church, J. A. (2021, 4). Fifty Year Trends in Global Ocean Heat Content Traced to Surface Heat Fluxes in the Sub-Polar Ocean. *Geophysical Research Letters*, *48*(e2020GL091439), 1 – 13. doi: 10.1029/2020gl091439

Sohail, T., Zika, J. D., Irving, D. B., & Church, J. A. (2022). Observed poleward freshwater transport since 1970. *Nature*, *602*(7898), 617–622. doi: 10.1038/s41586-021-04370-w

Winton, M., Anderson, W. G., Delworth, T. L., Griffies, S. M., Hurlin, W. J., & Rosati, A. (2014). Has coarse ocean resolution biased simulations of transient climate sensitivity? *Geophysical Research Letters*, *41*(23), 8522–8529. doi: 10.1002/2014gl061523

Yang, H., & Zhu, J. (2011). Equilibrium thermal response timescale of global oceans. *Geophysical Research Letters*, *38*(14), n/a–n/a. doi: 10.1029/2011gl048076